Thiol-Stabilized Atomically Precise, Superatomic Silver Nanoparticles for Catalyzing Cycloisomerization of Alkynyl Amines

Juanzhu Yan,[1] Jun Zhang,[2] Xumao Chen,[1] Sami Malola,[3] Bo Zhou,[1] Elli Selenius,[3] Xiaomin Zhang,[1] Peng Yuan,[1] Guocheng Deng,[1] Kunlong Liu,[1] Haifeng Su,[1] Boon K. Teo,[1] Hannu Häkkinen,[3*] Lansun Zheng[1] and Nanfeng Zheng[1*]

[1]State Key Laboratory for Physical Chemistry of Solid Surfaces, Collaborative Innovation Center of Chemistry for Energy Materials, and Engineering Research Center for Nano-Preparation Technology of Fujian Province, College of Chemistry and Chemical Engineering, Xiamen University, Xiamen 361005, China. *email: nfzheng@xmu.edu.cn

[2]School of Materials and Chemical Engineering, Anhui Jianzhu University, Hefei, Anhui 230601, PR China.

[3]Departments of Physics and Chemistry, Nanoscience Center, University of Jyväskylä, FI-40014 Jyväskylä, Finland. *email: hannu.j.hakkinen@jyu.fi

ABSTRACT

Both the electronic and surface structures of metal nanomaterials play critical roles in determining their chemical properties. However, the non-molecular nature of conventional nanoparticles makes it extremely challenging to understand the molecular mechanism behind many of their unique electronic and surface properties. In this work, we report the synthesis, molecular and electronic structures of an atomically precise nanoparticle, $[Ag_{206}L_{72}]^q$ (L = thiolate, halide; q = charge). With a four-shell $Ag_7@Ag_{32}@Ag_{77}@Ag_{90}$ Ino-decahedral structure having an nearly perfect D_{5h} symmetry, the metal core of the nanoparticle is co-stabilized by 68 thiolate and 4 halide ligands. Both electrochemistry and plasmonic absorption reveal the metallic nature of the nanoparticles, which is explained by density functional theory calculations. Electronically, the nanoparticle can be considered as a superatom, just short of a major electron shell closing of 138 electrons (q = -4). More importantly, many of ligands capping on the nanoparticle are labile due to their low-coordination modes, leading to high surface reactivity for catalyzing the synthesis of indoles from 2-ethynylaniline derivatives. The results exemplify the power of the atomic-precision nanocluster approach to catalysis in probing reaction mechanisms and in revealing the interplay of heterogeneous reactivities, electronic and surface structural dynamics, thereby providing ways for optimization.

Keywords: metal nanoclusters, atomically precise nanoparticles, nobel metal, superatom, nanocatalysis

INTRODUCTION

Metal nanoparticles have emerged as an important topic in materials research in view of their intriguing properties and wide-range applications in areas such as catalysis [1], electronics [2], bio-sensing [3] and nanomedicine [4], etc. Investigations have revealed that the size, shape and composition of these particles have a great influence on their properties [5-8]. Thus unravelling the hierarchical nature in nanostructured systems is vital to the development of nanomaterials and nanotechnology [9-12]. However, conventional nanoparticles are usually intrinsically heterogeneous and it is challenging to define their surface structures down to atomic precision, even with advanced transmission electron microscopy (TEM) and scanning-probe microscopies, therefore precluding studies of the precise correlation of particle structure and property [13-15]. In recent years, great advances have been made in the syntheses of metal nanoparticles with monodispersity, in particular, atomically precise nanoparticles with well-defined surface structures that bestows on them the potential to shed light on important issues in surface sciences [16-29].

In the case of catalysis, atomically precise metal nanoparticles loaded on solid support provide an ideal system for studying interfacial phenomena and surface reactivities in relation to catalytic mechanisms [25,30,31]. As is well known, the capping reagents not only inhibit nanoparticle overgrowth and aggregation owing to electrostatic or steric repulsion [32,33], but also determine the composition and structure of the resulting nanoparticles in a precise manner. At the same time, surface ligands play a critical role in catalysis because they determine the accessibility of the reactant(s) to the nanoparticle surface [34]. On the basis of their crystal structures, study of the effect of the capping ligands on a particle surface can unveil adverse or favorable behavior in a catalytic reaction [31]. In essence, while the capping agents usually act as a physical barrier to restrict the access of reactants to the catalytic site, they can also be utilized to promote catalytic performance of nanocrystals [33]. However, few works have focused on the surface reactivity caused by the lability of capping agents on catalysis down to atomic precision.

In an attempt to gain insights with regards to the above-mentioned issues, we report herein the synthesis of a novel metal nanoparticle, formulated as $[Ag_{206}(SR)_{68}F_2Cl_2]^q$ (**1**, q = +2, +3, +4 and +5) where SR=cyclohexanethiol based on structure determination by single-crystal X-ray crystallography. The 206-metal-atom Ag nanoparticle can be structurally described as a multi-shell $Ag_7@Ag_{32}@Ag_{77}@Ag_{90}$ metal framework capped by 72 thiolated and halide ligands. The 116 Ag atoms in the nanoparticle kernel are arranged in an Ino-decahedron-shape framework with nearly perfect five-fold symmetry, while the Ag_{90} surface shell are in slightly distorted hexagonal close packing (*hcp*) arrangements relative to the Ag_{116} kernel. More importantly, the thiolated ligands capping on the Ag_{206} surface are labile due to their low-coordination modes, leading to high surface reactivity and catalytic behavior. The latter was modeled by the syntheses of indoles from 2-ethynylaniline derivatives. Based on the catalytic results, a reaction mechanism is proposed.

RESULTS AND DISCUSSION

Synthesis and characterization. To prepare the silver nanoparticles co-protected by thiolate and halide, the metal precursors (i.e., silver hexafluoroantimonate) were chemically reduced by sodium borohydride in the presence of cyclohexanethiol (RSH) and triethylamine in a mixed solvent of methanol and dichloromethane at 0°C (see Methods and SI for more details). The as-prepared product was characterized by electrospray ionization mass spectrometry (ESI-MS) in the positive ion mode. As shown in Fig. 1a, the obtained ESI-MS spectrum displayed a number of main peaks in the range of m/*z* from 5950 to 15300 with several ion species. The major mass peaks were identified as follows: $[Ag_{206}(SR)_{70-x}F_xCl_2]^{5+}$, $[Ag_{206}(SR)_{70-x}F_xCl_2]^{4+}$, $[Ag_{206}(SR)_{70-x}F_xCl_2]^{3+}$ and $[Ag_{206}(SR)_{70-x}F_xCl_2]^{2+}$ (x=0-4). The high-resolution mass spectra of **1** revealed a perfect match between the observed and the simulated isotopic distribution of $[Ag_{206}(SR)_{70-x}F_xCl_2]^{4+}$ and $[Ag_{206}(SR)_{70-x}F_xCl_2]^{3+}$ peaks (see insets in Fig. 1a). Besides, easy replacement of thiolates on **1** by F^- ions as well as other +1 small fragmented complexes were observed owing to electrostatic destabilization and spontaneous fragmentation of $[Ag_{206}(SR)_{70-x}F_xCl_2]^q$ (q = +2, +3, +4 and +5). The ESI-MS results indicated the presence of the $[Ag_{206}L_{72}]^q$ (L=SR, Cl and F) component in the crude product. Attempts to detect anionic species (negative q) in the anionic ESI-MS mode were unsuccessful. And transmission electron microscopic (TEM) analyses showed that the as-prepared Ag nanoparticles had a more-or-less uniform size (1.9 ± 0.2 nm,

Supplementary Fig. 1). It can be concluded that the crude product contains a high-purity 206-Ag-atom nanoparticles stabilized by peculiarly labile ligands. To determine the molecular structure, single crystals suitable for X-ray diffraction were grown by diffusing hexane into the dichloromethane solution of **1** at 0°C. The obtained dark single crystals crystallized in a monoclinic *I*2/a space group (Fig. 1b). Single-crystal structure analysis revealed the composition of $[Ag_{206}(SR)_{68}F_2Cl_2]^q$ (**1**) (Fig. 1c). The charge *q* cannot be determined due to disorders of the counterions (most likely halides with *q* = +4 based on the ESI-MS data) and the solvent molecules. Each nanoparticle is composed of 206 Ag atoms and 68 thiolates (SR) and 4 halide (F and Cl) .

Atomic structure. As revealed by single-crystal structure analysis, the metal framework in $[Ag_{206}(SR)_{68}F_2Cl_2]^q$ (**1**) can be described as a fivefold twinned Ino-decahedron of Ag_{206} with a four-shell $Ag_7@Ag_{32}@Ag_{77}@Ag_{90}$ structure. It is stabilized by 72 mixed ligands (Fig. 2a, b). The multi-shell $Ag_7@Ag_{32}@Ag_{77}$ structure can be described as follows. The innermost shell is the ν_1 decahedral (pentagonal bipyramidal) Ag_7 core (Fig. 2c). It is capped on its ten faces by ten ν_2 triangular Ag_6 facets, to produce the second shell of ν_2 Ino-decahedral Ag_{32} (Fig. 2d). The latter is further enclosed by the third shell of ν_3 Ino-decahedral Ag_{77} (Fig. 2e). These three shells constitute the Ag_{116} kernel with ten (111) facets and five (100) facets (the latter will be referred to as the belt at the equator).

It should be noted that this Ag_{116} Ino-decahedron is distinctly different from Marks' multiply twinned decahedra [35]. Nevertheless, the Ag_{116} kernel of Ag_{206} can be also deemed as a miniature fivefold twinned nanorod constructed from five conjoined single-crystalline elongated tetrahedra along fivefold aspect (Supplementary Fig. 2 and Supplementary Table 2), which is akin to the reported Ag_{374} nanoparticle [23]. The average Ag–Ag bond length of Ag_{116} kernel is 2.873 Å, slightly shorter than the Ag–Ag bond distance (2.889 Å) of bulk silver. To eliminate the 7.35° deficiency among five ideal single-crystalline grains in a fivefold twinned nanostructure, small deviations from planarity (a slight bulging) at the twinning boundaries appears to be the only readily discernible compensation for the solid-angle deficiency of the fivefold twinned Ag_{116} kernel. Careful analysis revealed that the fivefold twinning boundary (111) faces in the Ag_{116} kernel are not strictly planar (Supplementary Fig. 3). Within each shared (111) face, some Ag atoms deviate from the plane of their coplanar Ag set by up to 0.21 Å and their corresponding twisted angle up to 1.45°.

As expected, the adjacent shells of the ν_1 decahedral core and the ν_2 and ν_3 Ino-decahedral shells are in arranged *fcc* configurations. However, instead of a regular ν_4 Ino decahedral shell, the fourth (surface) shell of Ag_{90} adopts a twinned *hcp* arrangement, as depicted in Fig. 2f. Here each pentagonal pyramid is capped by a bowl-like Ag_{30} unit described as one half of a parabigyrate rhombicosidodecahedron (Johnson solid J73—a circumscribable 60 vertex figure) [36]. The five side (100) faces of the Ag_{116} kernel are each covered by five near planar Ag_6 units. In each Ag_6 unit, the silver atoms are arranged in somewhat irregular 2 × 3 patterns. Two Ag_{30} units and five Ag_6 ones are mutually connected to form the fourth shell of Ag_{90}, which can be described as a semiregular polyhedron with 10 ν_2 triangles, 50 squares, 5 irregular rectangles and 2 pentagons.

Apart from the characteristic fivefold twinned Ag_{206} metal framework, another interesting feature is the abundant and symmetric distribution of various ligands on surface layer. Each ligand is arranged along C_2 rotation axes in different directions. The ligand coordination modes are shown in Fig. 2 (different types of surface Ag polygons are color coded). Thus, each of the two apical (pink) pentagon is capped by a chloride (in red) atom (Fig. 2g). Ten thiolates cap 10 blue highly distorted ν_2 triangles (Fig. 2h). The S atoms are colored in yellow. Each square at the two apical and five side (100) square faces is capped by a tetradentate thiolate ligand (Fig. 2k, m and n, highlighted in khaki), with the exception that two severely distorted squares (Fig. 2k) are capped by fluorides (in pink). The irregular rectangle (highlighted in green) at the five pentagonal prismatic edges can be regarded as three coterminous irregular squares via sharing two common edges. Doubly bridging thiolates are situated on these common edges (Fig. 2j). The most important observation of the ligand binding modes is that most of them are highly asymmetric (Fig. 2 and Supplementary Fig. 4). For clarity, Ag-S, Ag-Cl or Ag-F distances longer than 2.7 Å are shown in Supplementary Fig. 4 (normal bond lengths are not shown). The only exception is the pentadentate chlorides coordinated to the apical Ag pentagons with average Ag-Cl distance of 3.091 Å (Fig. 2g, Supplementary Fig. 4 and Supplementary Table 2). Thus, the thiolates capping the highly distorted ν_2 triangles (Fig. 2h) may be considered as pentadentate with three short (normal) Ag-S bonds and two long Ag-S distances. The thiolates capping the square faces (Fig. 2k, m and n) are tetradentate with either three short (normal) Ag-S bonds and one long distance, or two short (normal) Ag-S bonds and two long Ag-S distances. In contrast to the thiolates, the fluorides capping the severely distorted silver squares (Fig. 2k and

Supplementary Table 2) are tridentate with two short (normal) Ag-F bonds and one long Ag-F distance. The average Ag-F bond distances are 2.604 Å. In this fashion, they may also be regarded as tridentate capping a silver triangle. Finally, Thiolates capping the shared edges of the three coterminous irregular squares (Fig. 2j) were also bonded to the inner Ag_{72} shell with average Ag-S distances at 2.658 Å. Apparently the observed asymmetric coordination modes of the ligands, as well as the longer-than-normal Ag-S, Ag-Cl and Ag-F bonds are results of the geometrical constraints imposed by the Ino decahedral Ag_{116}, kernel and the surface Ag_{90} shell, making them easy targets for attack and eventual replacement by other ligands (*vide infra*). The above analysis also demonstrates that thiolate-coordinated modes in thiol-stabilized Ag nanoparticles are different from that in thiol-stabilized Au particles.

Electronic structure. The free-electron count [37] of $[Ag_{206}(SR)_{68}F_2Cl_2]^q$ is 206-68-4-q = (134-q) electrons. ESI-MS data suggest that the cluster may bear charges of 2, 3, 4 and 5 (which correspond to 132, 131, 130 and 129 electrons) with q = +4 being the most abundant (Fig. 1a). Motivated by the rather high symmetry (D_5) and a near-spherical overall shape of particle **1**, we explored the electronic structure of **1** in various redox states (4- ≤ q ≤ 5+) via density functional theory (DFT) computations by using the real-space code GPAW [38]. It was found that the electronic density of states (DOS) is robust for a large variety of charge states of **1**. An example is shown in Fig. 3 for the charge of -4 that corresponds to 138 free electrons. The DOS shows a rather significant HOMO-LUMO energy gap of about 0.4 eV at that electron number, and projection of the electron states to spherical harmonics [37] shows grouping of states both below and above the gap into defined symmetries that follow the spherical shell model [39]. Below the HOMO-LUMO gap, a group of 23 states (46 electrons) of symmetries $3P^6$, $2F^{14}$, and $1I^{26}$ are found reaching the intermediate energy gap at 92 shell electrons. Above the HOMO-LUMO gap, 27 states (54 electrons) of 2G, 1J, 3D, and 4S symmetries are found spanning the next major shell up to 192 shell electrons. As illustrated in Fig. 3, the electron states show a degree of splitting and inter-mixing between different angular momentum sub-shells due to the distinct point-group symmetry and overall polyhedral shape of the core. To the best of our knowledge, particle **1** is one of the clearest examples of large ligand-stabilized noble metal nanoclusters that show such a distinct superatomic electronic structure.

Thermostability and optical properties. The thermogravimetric analysis (TGA) of crystalline samples of **1** was also carried out to confirm its composition (Supplementary Fig. 5a). A total weight loss of 26.15 wt% was in perfect agreement with the organic component of **1** (organic, 26.33 wt%; metal, 73.67 wt%). The thermal decomposition temperature of ligands was about 200°C, suggesting indirectly that **1** has a good thermal stability in the solid state. The UV-Vis spectrum (Fig. 4a) of Ag_{206} nanoparticles in CH_2Cl_2 displays one dominant plasmonic peak at 464 nm. The Ag_{206} absorption behavior is distinct from the molecule-like multiband absorption features of previously reported smaller thiolated Ag nanoclusters which displayed 6 intense peaks at 374, 411, 483, 535, 641 and 833 nm and 2 shoulder peaks at 590 and 689 nm [22]. The Ag_{206} solid was stable in air at room temperature for at least 2 months (Supplementary Fig. 5b).

Electrochemical result. A typical differential pulse voltammetry (DPV) response for the Ag_{206} nanoparticle dissolved in 0.1 M Bu_4NPF_6/CH_2Cl_2 at 0°C is given in Fig. 4b. It depicts a 12 evenly spaced (ΔV *is about 0.2 eV*) peaks characteristic of charge injection to, and abstraction from, the metal core, indicating that Ag_{206} is a multivalent redox species with no apparent HOMO-LUMO gap. The DFT calculations support this observation given that the electrochemistry achieves particle charge states that are less negative that 4- (i.e., the system is below the magic shell closing electron number of 138). The dense spacing of electronic states below 138 shell electrons (marked by a horizontal bar in Fig. 3) predicts a metallic behaviour in electrochemical experiments. Indeed, we calculated the total energy of particle **1** (without the solvent environment) in many charge states and found out that the energy behaves quadratically as a function of particle charge, with the optimal energy at $q = -3|e|$ (Supplementary Fig. 6). The energy minimum at this charge can be understood as the competition between the tendency to achieve the superatom shell closing (at $q = -4|e|$, *i.e*, 138 shell electrons) and the increased Coulomb repulsion between added negative charge. The quadratic behaviour of the total energy as a function of charge is a manifestation of metallic behaviour and indeed analogous to a completely classical case of charging a metal sphere [40]. The quadratic fit (Supplementary Fig. 6) yields an estimate for the constant charging energy of **1** as about 1.15 eV for each reduction/oxidation step. Comparison to the measured evenly spaced DPV peaks at about 0.2 eV separation (Fig. 4b) implies then that the dielectric environment of **1** in the reduction/oxidation process has an effective dielectric constant of about 6, which is a reasonable estimate taking into account both the thiol monolayer and the solvent. The metallic electrochemical charging has

been reported previously in the case of thiol-stabilized gold clusters with about 144-146 gold atoms [41,42] that are close to, but not yet achieving the magic shell electron count of 92 [43]. The metallic DPV behavior coincides with only one intense plasmonic peak in UV-Vis spectrum of Ag_{206} CH_2Cl_2 solution. Additional confirmation of the metallic character of the Ag_{206} core came from DFT calculations within the jellium description, where the positive background charge was smeared out uniformly in a polyhedral shape taken from the outermost Ag_{90} shell of the metal core (Supplementary Fig. 7). This calculation confirmed a similar electron shell structure (Supplementary Fig. 7a, b) to that found in the atomistic calculation, furthermore, the calculated optical absorption showed one strong plasmonic peak (Supplementary Fig. 7c), although clearly shifted from the experimental results due to the lack of Ag(4d) screening and missing effects from the ligand layer.

Surface reactivity and Catalytic performance of 1. The analysis of the Ag-S bond distances in **1**, as detailed above, revealed that most of the thiolates (22 SR) capping Ag_4 square faces tends to be two- or three-coordinated rather than four-coordinated (see Supplementary Fig. 4). These low-coordinated thiolates explain why the thiolated ligands can be easily replaced by halogen species, both as prepared in the solution phase as well as in the gas phase as observed in the ESI-MS measurements (Fig. 1a). To test the high surface reactivities of **1**, we also performed its ligand-exchange behavior with *tert*-butylacetylene (TBA). The result confirmed that these low-coordinated thiolates or halides are easy targets for attack and eventual replacement by TBA (Supplementary Figs. 8 and 9).

It occurs to us that the lability of protecting ligands on the surface of 1 could be exploited to perform catalytic reactions. The idea is to replace the surface thiolates or halides with a substrate (the reactant) which is subsequently activated by the Ag nanoparticle to undergo a certain reaction. On the basis of this hypothesis, we screened various reactions and discovered facile synthesis of indoles from 2-ethynylaniline derivatives using **1** as the catalyst. It is well known that 2-ethynylaniline derivatives have an acetylene terminal which has a strong affinity for, and could be selectively activated by, silver atoms. To this end, we prepared **1** and other reported nanoparticles (i.e. Ag_{44} and Ag_{374}) [22,23] loaded on inert support as model catalysts in order to compare their catalytic performance.

As envisioned, 5 mol% catalysts (calculated based on Ag atom, 1 wt% Ag_{206}/TiO_2) succeeded in accelerating the cycloisomerization reaction of N-(2-ethynylphenyl)-4-

methylbenzenesulfonamide (**2a**) to 1-tosyl-1H-indole (**2b**) at 60°C in 24 h, with a yield of 85% (Table 1, entry 7). The reaction conditions were optimized by exploring the effects of solvent, time, and temperature. The optimal conditions were identified as 5 mol% catalyst (1 wt% Ag_{206}/TiO_2) with a reaction time of 2 h at 80°C in toluene or chlorobenzene, providing the desired product with over 99% isolated yield. The reaction generally worked well in aprotic solvents (Table1, entries 1-6 and 8).

Given the optimal reaction conditions (Table 1, entries 5 and 9), we compared the three types of nanoparticles supported on TiO_2 or carbon. As shown in Table 2 (entries 1–9), while the blank test showed that no desired product was detected in the absence Ag species, the Ag_{206}/TiO_2 catalyst showed a much higher yield of over 99% in comparison to Ag_{44}/TiO_2 (37%) [22] or Ag_{374}/TiO_2 (38%) [23], as well as various Ag(I) precursors (<30%). We attribute the observed excellent catalysis of Ag_{206}/TiO_2 to the high surface reactivity and also unique electronic structure of Ag_{206} clusters (*vide infra*). The choice of the inert solid support had little influence on the catalytic activity (Table 2, entries 9 and 10). In order to evaluate the catalytic activity of Ag_{206}/TiO_2, the catalytic process of this model reaction was monitored. As illustrated in Fig. 4b and 4c, the Ag_{206}/TiO_2 catalyst displayed an extremely high activity and stability. Multiple runs of the reaction afforded the desired product with almost the same reaction activity and practically no obvious change in the particles size in the TEM images and UV-Vis spectra in a solid diffuse reflection mode (Supplementary Figs. 10 and 11), suggesting that the atomically precise structure of Ag_{206}/TiO_2 was robust under the catalytic conditions.

Based on the catalytic results described above, we propose a tentative mechanism for the Ag_{206}(**1**)$/TiO_2$-catalyzed cyclization reaction as shown in Supplementary Fig. 12 The premise here is that the labile (most likely the asymmetrically bonded) thiolates could be easily replaced by the reactants such as **2a** (Supplementary Fig. 13), furnishing an opportunity for the efficient contact between supported Ag_{206} catalyst and the reactant **2a**. The strong covalent binding between the acetylene terminal of the reactant **2a** and the surface Ag_4 squares of **1** could trigger the cyclization reaction to form indole products. It is likely that the activation process, as well as the catalytic activity is highly dependent on the surface reactivities and electron properties of silver nanoparticle. Interestingly, the DPV result of **1** also suggested that this nanoparticle was indeed a multivalent redox species; furthermore, at least four charge states of +5, +4, +3 and +2 were observed in the ESI-MS. These results imply that the Ag_{206} nanocluster (**1**) can switch from

one valence state to another, thereby facilitating the activation of carbon-carbon triple bond of **2a**. This catalytic cycle is indirectly supported by the structures of a number of stable reaction intermediates of an Ag_4-cluster-triggered cyclization of various acetylene-containing organic molecules to form indoles and other heteroaromatics [44].

CONCLUSION

In this study, the $[Ag_{206}(SR)_{68}F_2Cl_2]^q$ (**1**) nanoparticle, was synthesized in high yield and structural characterized by X-ray crystallography, ESI-MS, TEM and UV-Vis spectroscopy. The Ag_{206} nanoparticle **1** can be described as a four concentric core-shell structure of $Ag_7@Ag_{32}@Ag_{77}@Ag_{90}L_{72}$ (L= SR, Cl and F). The Ag atoms are arranged in approximately fivefold twinned pattern. The exposed Ag atoms and labile ligands on the surface of Ag_{206} units raise the potential utility of Ag_{206} nanoparticle in catalysis. Considering this hypothesis, 2-ethynylaniline derivatives were introduced as a substrate which effectively afforded the desired product in the presence of a catalytic amount of supported Ag_{206}. Subsequent the heterogeneous characteristics of the model reaction encouraged us to further test the recyclability of this system, it turned out that supported Ag_{206} catalyst was robust under the catalytic conditions. The multivalent redox of **1** was observed by DPV result and rationalized *via* DFT calculations. The results exemplify the power of the atomic-precision nanoparticle approach in revealing the interplay of catalysis, heterogeneous reactivity, electronic and surface structural dynamics in nanocatalysis. The catalysis of thiol-stabilized Ag nanoparticles is readily improved by tuning the bulkiness of their surface thiols and thus manipulating their binding strength on Ag nanoparticles.

METHODS

Preparation of $[Ag_{206}(SR)_{68}F_2Cl_2]^q$. In a typical preparation, 40 mg of silver hexafluoroantimonate was dissolved in 1 ml of methanol, followed by the addition of 4 ml of dichloromethane. The mixture was cooled to 0°C in an ice bath and 10 μL of cyclohexanethiol were then added. After 20-min stirring, 1 ml of an aqueous solution of sodium borohydride (40 mg/mL) and 50 μl of triethylamine were added quickly to the reaction mixture under vigorous stirring. The reaction mixture was aged for 12 h at 0°C. The aqueous phase was then removed. The organic phase was washed several times with water and evaporated for further analysis. Dark single crystals suitable for X-ray diffraction study were grown by a double-layer

of hexane/CH_2Cl_2 solution of crude product at 4°C for two weeks. The yield of **1** was ~25% (based on Ag).

Catalyst Preparation

Preparation of $(AgSR)_n$ polymer. 1 mmol cyclohexanethiol was added into 10 ml silver hexafluoroantimonate CH_2Cl_2 dispersion (0.1 M) under vigorous stirring. The suspension was aged at room temperature for 3 h. The resulting white precipitate, $(AgSR)_n$ polymer, was collected via centrifugation, washed with CH_2Cl_2 for five times and then dried in vacuum.

Preparation of 1 wt% Ag_{206}/TiO_2 and Ag_{206}/C. 5 ml CH_2Cl_2 solution of Ag_{206} nanoparticles (2 mg/mL) were slowly dropped into 20 ml CH_2Cl_2 dispersion of 1 g TiO_2 (Degussa P25) or C (Vulcan XC-72 carbon black) under vigorous stirring. The suspension was aged at room temperature for 6 h. The solid was collected via centrifugation, washed with CH_2Cl_2 for five times and then dried in vacuum.

Preparation of 1 wt% Ag_{44}/TiO_2 and Ag_{374}/TiO_2. Other monodisperse Ag_{44} and Ag_{374} nanoparticles were prepared according to the reported protocol [22,23]. The obtained nanoparticles were loaded on TiO_2 as same as the preparation of 1 wt% Ag_{206}/TiO_2.

Catalytic Experiments

Cyclization Reaction of N-(2-ethynylphenyl)-4-methylbenzenesulfonamide (**2a**) was carried out in a vial. For each reaction, a mixture of reactant, catalyst and solvent was placed into reactor. Then reaction mixture was vigorously stirred at the designed temperature for required time. After cooling the room temperature, the supernatant was collected via centrifugation, and purified by flash chromatography or preparative chromatography on a silica gel. The yields of 1-tosyl-1H-indole (**2b**) were calculated with reference to the obtained product. The product identification was carried out using ^1H and ^{13}C NMR (Supplementary Figs. 14-16).

DFT calculations

All the atomistic and jellium DFT computations were done by using the real-space code package GPAW [38]. The experimental crystal structure of $Ag_{206}(SR)_{68}F_2Cl_2$ (SR = cyclohexanethiol) was used as the starting point, and total energies of $[Ag_{206}(SR)_{68}F_2Cl_2]^q$ with $4- \leq q \leq 5+$ were evaluated via single-point calculations, *i.e.*, ignoring the structural relaxation. For a cluster of this size, this is a reasonable approximation. The electron-electron interactions were described by the PBE-functional. The real-space grid spacing was 0.25 Å. Auxiliary DFT calculations were done within the jellium description without explicit atoms, but smearing the positive background charge uniformly in a polyhedral shape taken from the outermost Ag_{90} layer in the core of (**1**). The real-space grid spacing in these calculations was set to 0.4

Å. The electronic structure of both the atomistic $[Ag_{206}(SR)_{68}F_2Cl_2]^q$ and jellium model of the core with q = 4- (corresponding to 138 free electrons) was analyzed via projection of the Kohn-Sham orbitals to spherical harmonics as described previously [37].

SUPPLEMENTARY DATA

Supplementary Data are available at NSR online.

ACKNOWLEDGEMENT

The computations were made at the CSC computing center in Espoo, Finland (Project jyy1713) and at the Barcelona Supercomputing Center (PRACE Project NANOMETALS).

FUNDING

We thank the National Key R&D Program of China (2017YFA0207302) and the National Natural Science Foundation of China (21731005, 21420102001, 21333008, 21390390) for financial support. The financial support (to B. T.) from *i*ChEM, Xiamen University and from National Innovation and Intelligence Introduction Base Program (to H. H.) is gratefully acknowledged. The work in University of Jyväskylä was supported by the Academy of Finland (266492 and Academy Professorship to H. H.).

Conflict of interest statement. None declared.

REFERENCES

1. Bell, AT. The Impact of Nanoscience on Heterogeneous Catalysis. *Science* 2003; **299**: 1688-91.
2. Takeda, K, Kamioka, J, Otsuka, T *et al.* A fault-tolerant addressable spin qubit in a natural silicon quantum dot. *Sci Adv* 2016; **2**: e1600694.
3. Saha, K, Agasti, SS, Kim, C *et al.* Gold Nanoparticles in Chemical and Biological Sensing. *Chem Rev* 2012; **112**: 2739-79.
4. Karimi, M, Ghasemi, A, Zangabad, SP *et al.* Smart micro/nanoparticles in stimulus-responsive drug/gene delivery systems. *Chem Soc Rev* 2016; **45**: 1457-501.
5. Jiang, W, Kim, BYS, Rutka, JT *et al.* Nanoparticle-mediated cellular response is size-dependent. *Nat Nanotech* 2008; **3**: 145-50.
6. Burda, C, Chen, XB, Narayanan, R *et al.* Chemistry and Properties of Nanocrystals of Different Shapes. *Chem Rev* 2005; **105**: 1025-102.
7. Sun, SH, Murray, CB, Weller, D *et al.* Monodisperse FePt Nanoparticles and Ferromagnetic FePt Nanocrystal Superlattices. *Science* 2000; **287**: 1989-92.
8. El-Sayed, MA. Small Is Different: Shape-, Size-, and Composition-Dependent Properties of Some Colloidal Semiconductor Nanocrystals. *Acc Chem Res* 2004; **37**: 326-33.
9. Shipway, AN and Katz, E and Willner, I. Nanoparticle Arrays on Surfaces for Electronic, Optical, and Sensor Applications. *ChemPhysChem* 2000; **1**: 18-52.
10. Niemeyer, CM. Nanoparticles, Proteins, and Nucleic Acids: Biotechnology Meets Materials Science. *Angew Chem, Int Ed* 2001; **40**: 4128-58.

11. Lu, K and Lu, L and Suresh, S. Strengthening Materials by Engineering Coherent Internal Boundaries at the Nanoscale. *Science* 2009; **324**: 349-52.
12. Bartels, T and Choi, JG and Selkoe, DJ. α-Synuclein occurs physiologically as a helically folded tetramer that resists aggregation. *Nature* 2011; **477**: 107-10.
13. Xu, WL, Kong, JS, Yeh, YTE *et al.* Single-molecule nanocatalysis reveals heterogeneous reaction pathways and catalytic dynamics. *Nat Mater* 2008; **7**: 992-96.
14. Yang, XF, Wang, AQ, Qiao, BT *et al.* Single-Atom Catalysts: A New Frontier in Heterogeneous Catalysis. *Acc ChemRes* 2013; **46**: 1740-48.
15. Somorjai, GA, Contreras, AM, Montano, M *et al.* Clusters, surfaces, and catalysis. *Proc Natl Acad Sci* 2006; **103**: 10577-83.
16. Jadzinsky, PD, Calero, G, Ackerson, CJ *et al.* Structure of a Thiol Monolayer-Protected Gold Nanoparticle at 1.1 Å Resolution. *Science* 2007; **318**: 430-33.
17. Joshi, CP, Bootharaju, MS, Alhilaly, MJ *et al.* $[Ag_{25}(SR)_{18}]^-$: The "Golden" Silver Nanoparticle. *J Am Chem Soc* 2015; **137**: 11578-81.
18. Yan, JZ, Su, HF, Yang, HY *et al.* Total Structure and Electronic Structure Analysis of Doped Thiolated Silver $[MAg_{24}(SR)_{18}]^{2-}$ (M = Pd, Pt) Clusters. *J Am Chem Soc* 2015; **137**: 11880-83.
19. Jin, RC, Zeng, CJ, Zhou, M *et al.* Atomically Precise Colloidal Metal Nanoclusters and Nanoparticles: Fundamentals and Opportunities. *Chem Rev* 2016; **116**: 10346-413.
20. Yamazoe, S and Koyasu, K and Tsukuda, T. Nonscalable Oxidation Catalysis of Gold Clusters. *Acc Chem Res* 2014; **47**: 816-24.
21. Zeng, CJ, Chen, YX, Kirschbaum, K *et al.* Emergence of hierarchical structural complexities in nanoparticles and their assembly. *Science* 2016; **354**: 1580-84.
22. Yang, HY, Wang, Y, Huang, H *et al.* All-thiol-stabilized Ag_{44} and $Au_{12}Ag_{32}$ nanoparticles with single-crystal structures. *Nat Commun* 2013; **4**: 2422.
23. Yang, HY, Wang, Y, Chen, X *et al.* Plasmonic twinned silver nanoparticles with molecular precision. *Nat Commun* 2016; **7**: 12809.
24. Desireddy, A, Conn, BE, Guo, J *et al.* Ultrastable silver nanoparticles. *Nature* 2013; **501**: 399-402.
25. Ren, LT, Yuan, P, Su, HF *et al.* Bulky Surface Ligands Promote Surface Reactivities of $[Ag_{141}X_{12}(S\text{-}Adm)_{40}]^{3+}$ (X = Cl, Br, I) Nanoclusters: Models for Multiple-Twinned Nanoparticles. *J Am Chem Soc* 2017; **139**: 13288-91.
26. Gary, DC, Flowers, SE, Kaminsky, W *et al.* Single-Crystal and Electronic Structure of a 1.3 nm Indium Phosphide Nanocluster. *J Am Chem Soc* 2016; **138**: 1510-13.
27. Lovat, G, Choi, B, Paley, DW *et al.* Room-temperature current blockade in atomically defined single-cluster junctions. *Nat Nanotech* 2017; **12**: 1050-54.
28. Nguyen, T-AD, Jones, ZR, Leto, DF *et al.* Ligand-Exchange-Induced Growth of an Atomically Precise Cu_{29} Nanocluster from a Smaller Cluster. *Chem Mater* 2016; **28**: 8385-90.
29. Qian, EA, Wixtrom, AI, Axtell, JC *et al.* Atomically precise organomimetic cluster nanomolecules assembled via perfluoroaryl-thiol SNAr chemistry. *Nat Chem* 2017; **9**: 333-40.
30. Chong, HB and Zhu, MZ. Catalytic Reduction by Quasi-Homogeneous Gold Nanoclusters in the Liquid Phase. *ChemCatChem* 2015; **7**: 2296-304.
31. Wang, Y, Wan, XK, Ren, LT *et al.* Atomically Precise Alkynyl-Protected Metal Nanoclusters as a Model Catalyst: Observation of Promoting Effect of Surface Ligands on Catalysis by Metal Nanoparticles. *J Am Chem Soc* 2016; **138**: 3278-81.
32. Moore, TL, Rodriguez-Lorenzo, L, Hirsch, V *et al.* Nanoparticle colloidal stability in cell culture media and impact on cellular interactions. *Chem Soc Rev* 2015; **44**: 6287-305.
33. Campisi, S, Schiavoni, M, Chan-Thaw, C *et al.* Untangling the Role of the Capping Agent in Nanocatalysis: Recent Advances and Perspectives. *Catalysts* 2016; **6**: 185.
34. Liu, PX, Qin, RX, Fu, G *et al.* Surface Coordination Chemistry of Metal Nanomaterials. *J Am Chem Soc* 2017; **139**: 2122-31.
35. Marks, LD. Surface structure and energetics of multiply twinned particles. *Philos Mag A* 1984; **49**: 81-93.

36. Johnson, NW. Convex polyhedra with regular faces. *Canad J Math* 1966; **18**: 169-200.
37. Walter, M, Akola, J, Lopez-Acevedo, O *et al.* A unified view of ligand-protected gold clusters as superatom complexes. *Proc Natl Acad Sci* 2008; **105**: 9157-62.
38. Enkovaara, J, Rostgaard, C, Mortensen, JJ *et al.* Electronic structure calculations with GPAW: a real-space implementation of the projector augmented-wave method. *J Phys: Condens Matter* 2010; **22**: 253202.
39. Martin, TP, Bergmann, T, Goehlich, H *et al.* Shell structure of clusters. *J Phys Chem* 1991; **95**: 6421-29.
40. Häkkinen, H and Barnett, RN and Landman, U. Electronic Structure of Passivated $Au_{38}(SCH_3)_{24}$ Nanocrystal. *Phys Rev Lett* 1999; **82**: 3264-67.
41. Hicks, JF and Miles, DT and Murray, RW. Quantized Double-Layer Charging of Highly Monodisperse Metal Nanoparticles. *J Am Chem Soc* 2002; **124**: 13322-28.
42. Quinn, BM, Liljeroth, P, Ruiz, V *et al.* Electrochemical Resolution of 15 Oxidation States for Monolayer Protected Gold Nanoparticles. *J Am Chem Soc* 2003; **125**: 6644-45.
43. Lopez-Acevedo, O, Akola, J, Whetten, RL *et al.* Structure and Bonding in the Ubiquitous Icosahedral Metallic Gold Cluster $Au_{144}(SR)_{60}$. *J Phys Chem C* 2009; **113**: 5035-38.
44. He, X, Xue, Y, Li, C-C *et al.* Synthesis of stable polymetalated aromatic complexes through metal–macrocycle capsule-triggered cyclization. *Chem Sci* 2018; **9**: 1481-1487.

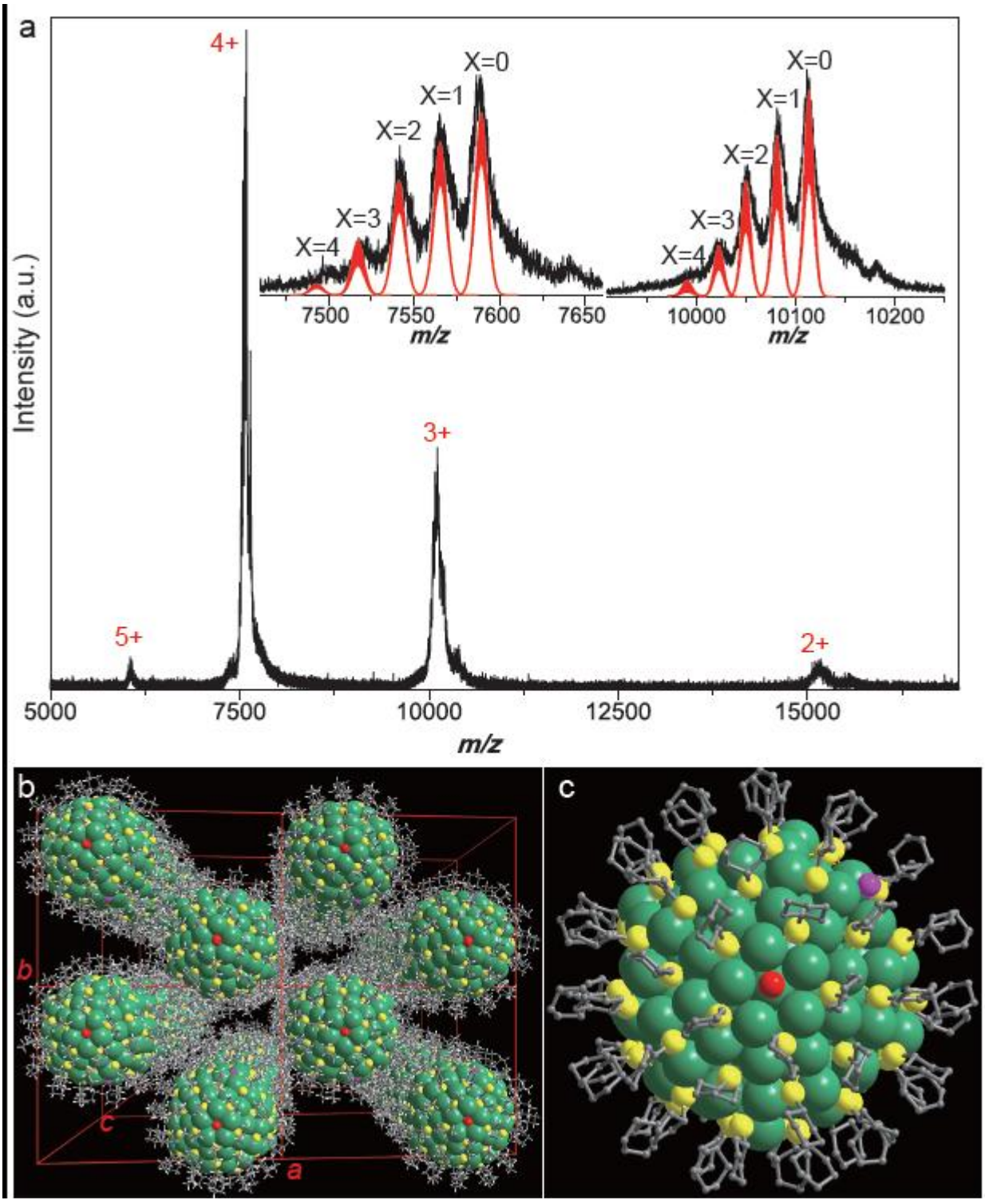

Figure 1. Representative characterizations of the $[Ag_{206}(SR)_{70-x}F_xCl_2]^q$ (1, x=0-4) nanoparticle. (**a**) ESI MS of as-prepared crude product of **1** dissolved in CH_2Cl_2. Insets show the comparison of the experiment (in black) and simulated (in red) isotopic patterns of the MS of $[Ag_{206}(SR)_{70-x}F_xCl_2]^{4+}$ (left) and $[Ag_{206}(SR)_{70-x}F_xCl_2]^{3+}$ (right). (**b**) Interparticle self-assembly

demonstration of **1** in crystal lattice. Color codes: green, Ag; yellow sphere, S; red, Cl; Pink, F; grey, C; and white sphere, H. (**c**) Overall structure of **1**.

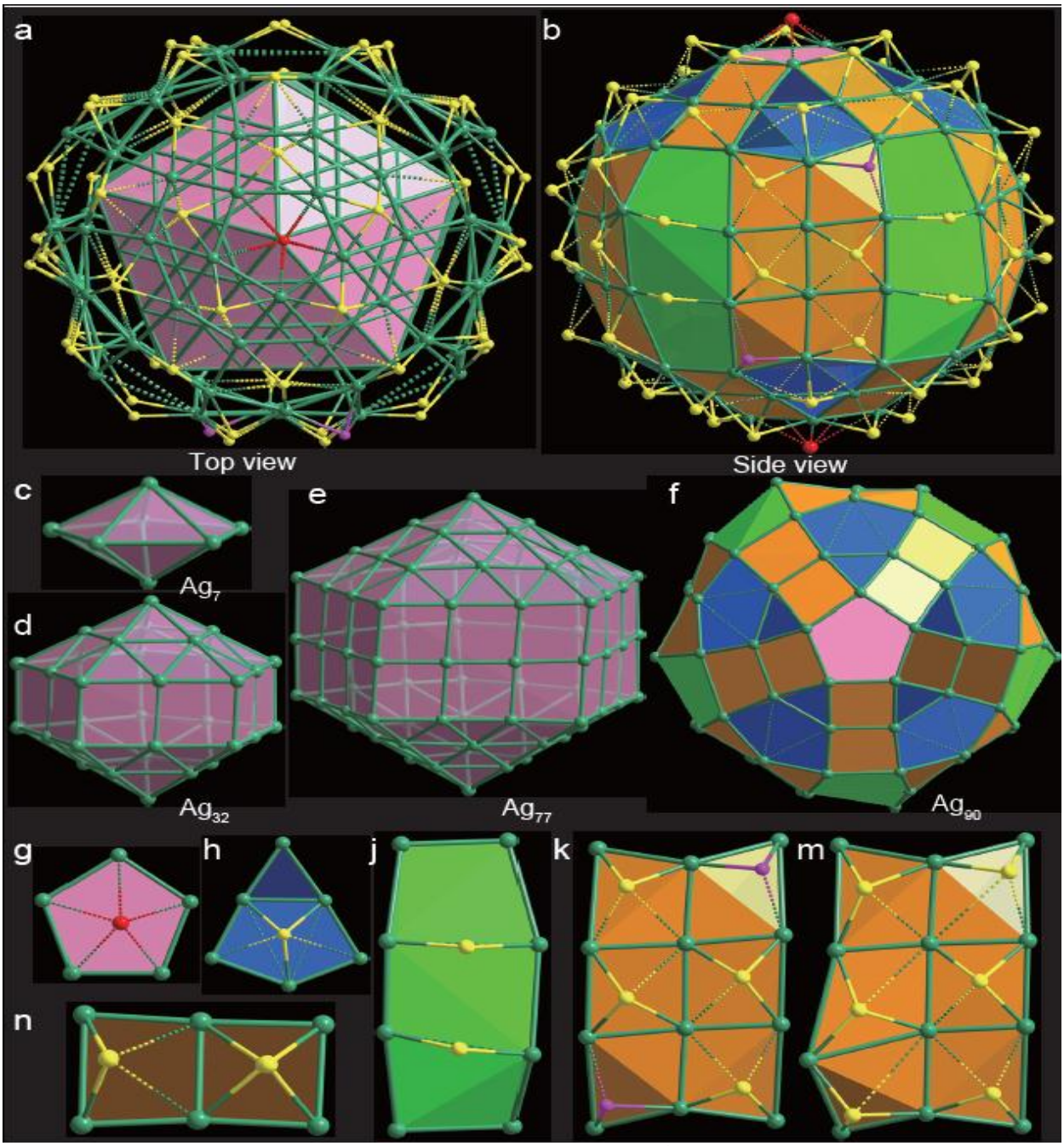

Figure 2. Geometrical structure of the $[Ag_{206}(SR)_{68}F_2Cl_2]^q$ nanoparticle. (**a** and **b**) **1** nanoparticle with the R groups omitted for clarity: top view (**a**) and side view (**b**). (**c-f**) Four-shell Ag_{206} framework: 1st Ag_7 decahedron (**c**), 2nd Ag_{32} υ_2 Ino decahedron (**d**), 3rd Ag_{77} υ_3 Ino decahedron (**e**) and 4th Ag_{90} polyhedron (**f**, highlighted in different color according to ligand coordination mode). (**g**) Chloride situated on pink pentagons at the poles. **h**. Three-fold coordinated thiolate centered on 6-Ag-atom triangle (highlighted in blue in panels **f**, **h**). (**k, m and n**) Two tetradentate thiolates severally capped on squares (highlighted in khaki in panels).

(**j**) Bridged thiolates capped on two common edges (dotted line) of green irregular rectangles. Ag-S and Ag-F bond lengths longer than 2.7 Å are coded in dot line. Color codes: green, Ag; yellow sphere, S; red, Cl; and Pink, F.

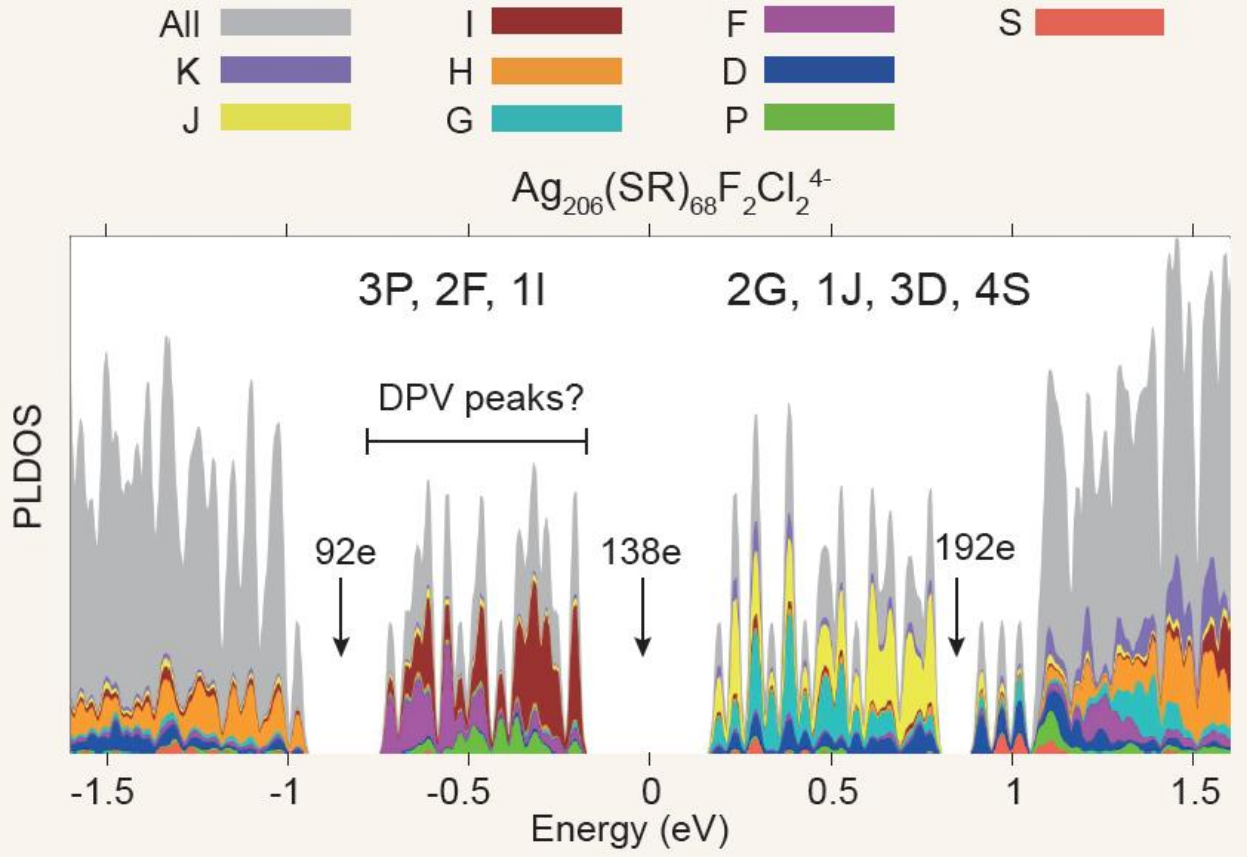

Figure 3. DFT characterization of the electronic shell structure of nanoparticle 1. Projection of the electronic density of states onto spherical harmonics (Y_{lm}) in the charge state of -4 shows a large HOMO-LUMO energy gap (centered around zero energy) that is reached at the magic number of 138 shell electrons. Likewise, other shell closings at 92 and 192 electrons are depicted. The angular momentum subshells are marked on the top of the figure and the coloring for the Y_{lm} components is shown in the legend. In the DPV experiment, electron states just below the HOMO energy are redox-cycled, as marked.

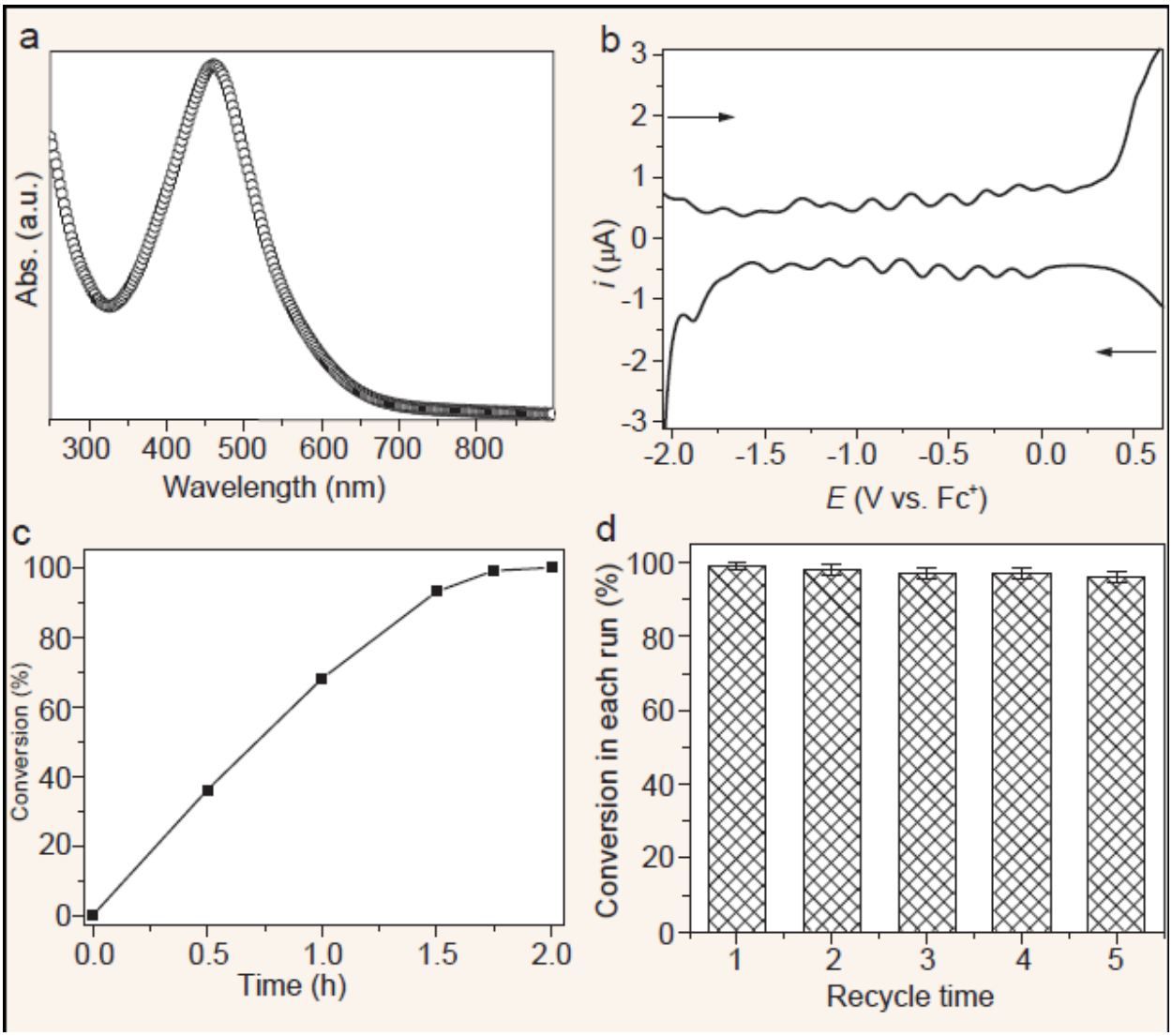

Figure 4. Characterization and catalytic properties of the $[Ag_{206}(SR)_{70-x}F_xCl_2]^q$ (1, x=0-4) nanoparticle. (**a**) UV-Vis spectrum of 1 dissolved in CH_2Cl_2. (**b**) Differential pulse voltammetry (DPV) responses of **1** for 1 in 0.1 M Bu_4NPF_6 in degassed CH_2Cl_2. **(c**) Catalytic performances of 1 wt% Ag_{206}/TiO_2 recorded at different reaction time points for the first run. (**d**) Recyclability of supported **1** (conversion of **2a**) in terms of activity.

Table 1. Optimization of Catalytic Conditions.

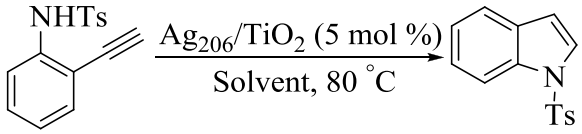

2a **2b**

Entry	Solvent	Time (h)	Yield[†] (%)
1	ethanol	6	70
2	acetonitrile	6	72
3	1,2-dichloroethane	2.5	>99
4	chloroform	2.5	>99
5	toluene	2	>99
6[‡]	chlorobenzene	24	trace
7[§]	chlorobenzene	24	69
8	chlorobenzene	2	>99

[†] Estimated by ^{1}H NMR.

[‡,§] Reaction temperature: room temperature (25°C) ([‡]), and 60°C ([§]).

Table 2. A comparison of activities for different catalysts. [†]

Entry	Catalyst	Time (h)	Yield [‡] (%)
1	TiO_2	12	trace
2	C	12	trace
3	$AgNO_3$	2	trace
4	$AgBF_4$	2	27
5	$AgSbF_6$	2	29
6	$(AgSR)_n$ polymer	2	7
7	Ag_{44}/TiO_2	2	37
8	Ag_{374}/TiO_2	2	38
9	Ag_{206}/TiO_2	2	>99
10	Ag_{206}/C	2	>99

[†] Reaction conditions: 80°C, [**2a**] = 0.1 M, chlorobenzene as solvent, 5 mol% catalyst, SR = cyclohexanethiolate.

[‡] Estimated by ^{1}H NMR.